

Non-isothermal direct bundle simulation of SMC compression molding with a non-Newtonian compressible matrix*

Nils Meyer^{a,b}, Sergej Ilinzeer^{a,c}, Andrew N. Hrymak^d, Frank Henning^{a,c}, Luise Kärger^a

^aKarlsruhe Institute of Technology (KIT), Institute of Vehicle System Technology, Karlsruhe, BW, Germany

^bUniversity of Augsburg, Institute of Materials Resource Management, Augsburg, BY, Germany

^cFraunhofer Institute for Chemical Technology (ICT), Pfinztal, BW, Germany

^dWestern University, Dept. of Chemical & Biochemical Engineering, London, ON, Canada

Abstract

Compression molding of Sheet Molding Compounds (SMC) is a manufacturing process in which a stack of discontinuous fiber-reinforced thermoset sheets is formed in a hot mold. The reorientation of fibers during this molding process can be either described by macroscale models based on Jeffery's equation or by direct mesoscale simulations of individual fiber bundles. In complex geometries and for long fibers, direct bundle simulations outperform the accuracy of state-of-the-art macroscale approaches in terms of fiber orientation and fiber volume fraction. However, it remains to be shown that they are able to predict the necessary compression forces considering non-isothermal, non-Newtonian and compaction behavior. In this contribution, both approaches are applied to the elongational flow in a press rheometer and compared to experiments with 23% glass fiber volume fraction. The results show that both models predict contributions to the total compression force and orientation reasonably well for short flow paths. For long flow paths and thick stacks, complex deformation mechanisms arise and potential origins for deviation between simulations models and experimental observations are discussed. Furthermore, Jeffery's basic model is able to predict orientations similar to the high-fidelity mesoscale model. For planar SMC flow, this basic model appears to be even better suited than the more advanced orientation models with diffusion terms developed for injection molding.

Keywords: Compression Molding, Sheet Molding Compound, Discontinuous Fiber Reinforcement

1. Introduction

Sheet molding compounds (SMC) are discontinuously reinforced polymer composites that are produced in a compression molding process. The process allows cost-efficient production of complex parts because the material can flow in complex shapes and forms features, such as ribs, beads, or overmolded inserts. The fibers are usually about 25 mm long, which is much longer than in injection molding processes and leads to better mechanical performance. However, these long fibers pose challenges to simulation and modeling, even after decades of research on SMC compression molding dating back to the 1980s [1, 2, 3].

The first step in SMC manufacturing is the production of prepregged material on a SMC line. Two polymer foils are coated with a thermosetting matrix, fiber bundles are introduced between the foils and the resulting sandwich is coiled for storage. A maturing processes increases the resin viscosity during storage, which enables further processing of the sheets

by cutting and stacking. An initial stack of SMC sheets at room temperature is then formed by compression molding in a heated mold. This process generally involves heat transfer, curing of the thermosetting resin, suspension flow with reorientation of fiber bundles, fiber-matrix separation effects, weld-line formation, friction at the mold and the release of air trapped in voids of the initial stack. It is desirable to simulate such effects to account for them during mold design and use the results in subsequent structural simulations [4, 5].

Early models describe the SMC flow with two-dimensional approaches, as SMC parts often have a planar shape. Silva-Nieto et al. [1] assumed an isothermal Newtonian material without fiber reorientation and solved the flow based on a Poisson type equation for the pressure. Tucker and Folgar [2] proposed a thickness averaged Hele-Shaw model that is solved by the finite element method (FEM) with the incorporation of heat transfer, non-Newtonian viscosity and curing. The authors advanced the Lagrangian mesh with the flow front and remeshed the domain during the simulation. They compared non-Newtonian isothermal simulations to experimental results and concluded that isothermal Newtonian models are limited to sufficiently thin parts [6]. Osswald and Tucker [7] solved the two-dimensional compression molding problem on complex domains with finite elements and the boundary element method to mitigate the need of a finite element mesh [8]. Barone and Caulk [3] performed experiments with colored SMC sheets to

*NOTICE: this is the author's version of a work that was accepted for publication in Journal of Non-Newtonian Fluid Mechanics. Changes resulting from the publishing process, such as peer review, editing, corrections, structural formatting, and other quality control mechanisms may not be reflected in this document. Changes may have been made to this work since it was submitted for publication. A definitive version was subsequently published in Journal of Non-Newtonian Fluid Mechanics, 310, 104940, (December 2022), <https://doi.org/10.1016/j.jnnfm.2022.104940>

analyze flow kinematics and observed that the flow rather resembles a *plug-flow* instead of the parabolic profile with no-slip conditions at mold walls used in the previous models. They propose a hydrodynamic friction model for the contact between SMC and mold, which is motivated by a small heated lubrication layer close to the mold surfaces. Efforts to parameterize such plug-flow models and obtain correct compression forces were presented by several authors [9, 10, 11, 12, 13]. A recent review on the numerical modeling of SMC compression molding is given by Alnersson et al. [14].

Fibers reorient during compression molding and models for the reorientation of short, rigid fibers are often based on Jeffery's equation [15]. Fiber orientation tensors were introduced to simplify the description of multiple suspended fibers [16] and several empirical parameters for fiber interaction [17], reduced strain [18] and anisotropic interaction [19] were introduced to enhance Jeffery's equation. These models are successfully applied to injection molding applications, but generally the prerequisites do not strictly apply for SMC. Thus, microscale models may be used to perform computational rheology experiments [20], to fit macroscopic model parameters [21, 22, 23], or to investigate critical molding areas [24, 25]. The simulation of all fibers in a component is computationally still unfeasible, but several authors [22, 26, 27, 28] observed that fibers typically stay in a bundled configuration during SMC compression molding. A compression molding simulation on component scale with individual bundles at mesoscale was demonstrated in [29] and showed accurate results of the fiber architecture, when compared to CT scans. The mesoscale simulation accounts for anisotropic flow, varying fiber volume content and can predict fiber matrix segregation in confined regions [30]. However, the previous work [29, 31, 30] simplified the rheology and focused on fiber architecture, but did not validate results of the computed pressures yet.

Therefore, this contribution aims at simulating a non-isothermal, non-Newtonian and compressible compression molding process on the mesoscale, i.e. resolving fiber bundles. For reference, a one-dimensional macroscale model is formulated and solved. The simulation results are compared to a flow in a rheological tool equipped with several pressure sensors along the flow path of SMC.

2. Experiments

The SMC under investigation is based on an unsaturated polyester-polyurethane hybrid (UPPH) resin that was developed to improve co-molding with unidirectional carbon fiber patches [32]. It has a glass fiber volume fraction of 23% with 25 mm fiber length. The fibers are grouped in bundles with 200 fibers each in a Multistar 272 multi-end roving by Johns Manville.

2.1. Transverse thermal properties

Thermal properties of uncured UPPH GF-SMC are determined from temperature measurements in a stack of SMC sheets. Ten sheets of 50 mm x 50 mm x 1.1 mm are stacked

Property	Value
Thermal conductivity κ	0.163 W m ⁻¹ °C ⁻¹
Gap conductance k	403 W m ⁻² °C ⁻¹

Table 1: Transverse thermal properties of UPPH-GF SMC in B-staged state.

to a total stack height $H = 11$ mm. Thermocouples are positioned centrally between each layer pair during stacking and the so prepared stack is embedded in a glass wool insulation fitting the stack with sensors (see Figure 1). The first sensor T1 is located on the bottom surface of the stack, so that it is located between mold and stack when the stack is placed on a heated mold surface at 145 °C. A small weight on top of this configuration ensures proper contact.

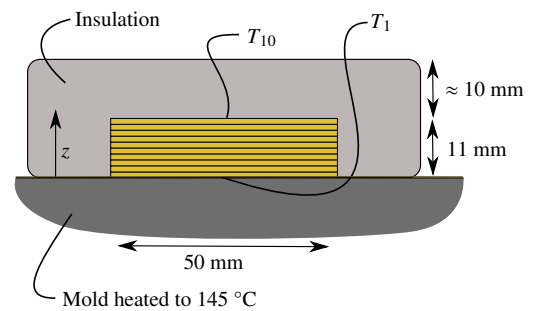


Figure 1: Setup for the evaluation of the transverse heat conductivity: Ten sheets of SMC are stacked with temperature sensors (T_1 to T_{10}) located centrally between each layer. The stack is embedded in glass wool insulation and then placed on a heated steel plate.

The specific heat capacity c_p is approximately 1530 J kg⁻¹ K⁻¹, which is estimated from data of the resin [33] and glass by rule of mixture. The transient heat transfer is approximated as a one-dimensional process transverse to the sheets

$$\rho c_p \frac{\partial T}{\partial t} = \kappa \frac{\partial^2 T}{\partial z^2} \quad z \in [0, H] \quad (1)$$

with the boundary conditions

$$\kappa \frac{\partial T}{\partial z} = 0 \quad z = H \quad (2)$$

$$\kappa \frac{\partial T}{\partial z} = -k(T_M - T) \quad z = 0 \quad (3)$$

as well as a constant mold temperature $T_M = 145$ °C, the gap conductance k and the thermal conductivity κ . Initially, the temperature T is homogeneous at $T_0 = 24$ °C. An optimal fit to the measured data is obtained by solving the initial boundary value problem for an initial guess of κ and k , computing a scalar squared error and minimizing the error iteratively. The experimental results and the optimal fit are shown in Figure 2. The corresponding parameters are summarized in Table 1.

2.2. Viscosity of the SMC paste

Specimens for viscosity measurement of the SMC paste are prepared by filling the paste in a mold instead of processing it on the SMC line. The mold is filled up to approximately

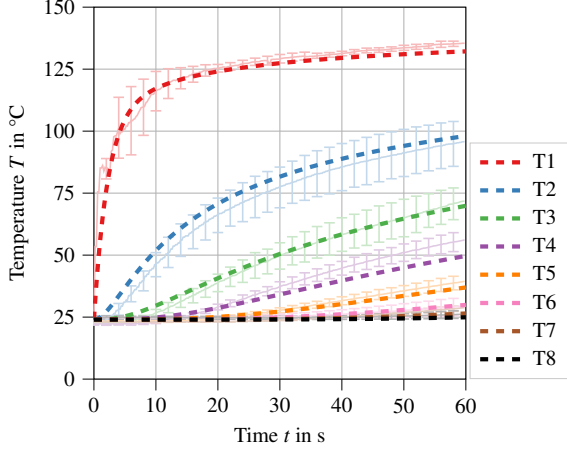


Figure 2: Measured temperatures (light solid lines with error bars indicating standard deviation) and best fit based on one-dimensional heat transfer equation (dark dashed lines) for sensors T1-T8. Sensors T9 and T10 are excluded, as they do not detect any noticeable temperature change.

1 mm thickness and sealed with styrene-tight foil. The paste is matured for two weeks at room temperature similar to the SMC for molding. Round coupons of 25 mm diameter are cut from the thickened paste and placed in a Anton Paar MCR501 rheometer in plate-plate configuration.

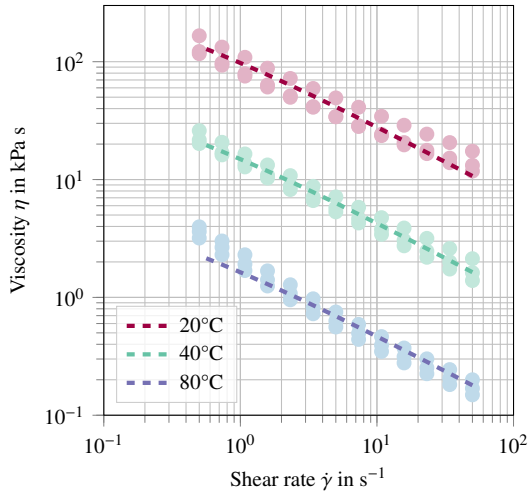


Figure 3: Measured viscosities at different temperatures (light dots) and best fit to viscosity model (dark dashed lines) given in Equation (4).

The viscosity as measured in oscillatory mode at 20 °C, 40 °C and 80 °C for three specimens each. While the peroxide initiator starts to create free radicals at 60 °C, significant fast cross-linking occurs typically at 100 °C and the temperatures are chosen to cover the relevant temperature range for the uncured resin paste. The measured viscosity shows typical power-law behavior. As the power-law behavior has a singularity at zero shear rate, a Cross-WLF-like model

$$\eta = \frac{\eta_0}{1 + \left(\frac{\dot{\gamma}}{\dot{\gamma}_0}\right)^{1-n}} \quad \text{with} \quad \eta_0 = D_1 e^{\frac{-\alpha_1(T-T^*)}{\alpha_2+(T-T^*)}} \quad (4)$$

and with a fixed transition shear rate $\dot{\gamma}_0 = 0.1$ is employed to

Property	Value
Reference viscosity D_1	72 kPa s
Transition shear rate $\dot{\gamma}_0$	0.1
Power law coefficient n	0.385
Glass transition temperature T^*	40.73 °C
Fitting parameter α_1	7.94
Fitting parameter α_2	105.96 °C

Table 2: Viscous properties of UPPH paste in B-staged state.

limit the viscosity at small shear rates. The power-law coefficient n , transition shear rate $\dot{\gamma}_0$ and parameters T^* , D_1 , α_1 , α_2 are fitted to the experimental results. These parameters should not be considered strictly as Cross-WLF parameters, as there is no plateau and the model is mainly chosen to smoothly transition to a finite viscosity as the shear rate approaches zero. The fit is obtained by minimizing the sum of squares of the normalized least-squares error at each measured temperature for all specimens. The experimental results and the optimal fit is shown in Figure 3. The corresponding parameters are summarized in Table 2.

2.3. Press rheometer trials

Compression trials are performed using a tool with a length L of 800 mm and a width W of 450 mm. The initial stacks always fill the entire width and are aligned to one end of the mold, while the length (and therefore mold coverage) varies between 25% and 100% (see gray regions in Figure 4). The mold is equipped with several pressure sensors (6167ASP by Kistler Instrumente GmbH, Sindelfingen, Germany) along the flow direction. The color-coded locations in Figure 4 are active during the trials in this work. The mold is heated to 145 °C and mounted to a hydraulic press with parallelism control (COMPRESS PLUS DCP-G 3600/3200 AS by Dieffenbacher GmbH Maschinen- und Anlagenbau, Eppingen, Germany). All trials are performed with a constant closing speed of $\dot{h} = -1 \text{ mm s}^{-1}$ and a maximum compression force $F_{\text{max}} = 4400 \text{ kN}$.

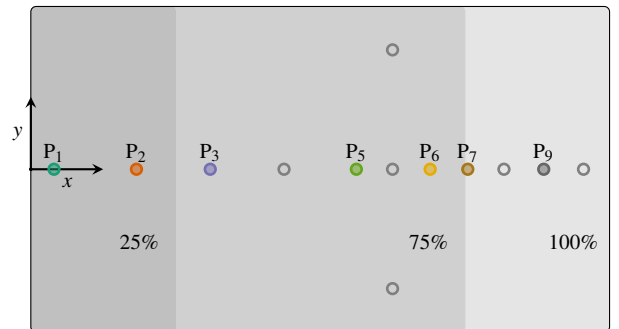


Figure 4: Press rheometer (800 mm x 450 mm) with pressure sensor locations. Active pressure sensor locations are color-coded and labeled P_s , alternate mounting positions are drawn as gray circles.

2.3.1. Hydrodynamic mold friction

The press rheometer enables a characterization of the hydrodynamic friction between SMC and the molds caused by the

lubrication layer. Assuming an ideal incompressible plug-flow in the tool, i.e. $\partial v_x / \partial z = 0$, friction stresses can be computed from the pressure differences between sensor pairs. The force balance for SMC between two sensors at position Δx_s with pressure p_s and position Δx_{s+1} with pressure p_{s+1} reads

$$2\tau(x_{s+1} - x_s)W = hW(p_{s+1} - p_s) \quad (5)$$

with the average friction shear stress τ and the current thickness of SMC h (see inset of Figure 5). Therefore

$$\tau = \frac{h(p_{s+1} - p_s)}{2(x_{s+1} - x_s)} \quad (6)$$

holds. The corresponding slip velocity v_s at a mid point between two sensors can be approximated from the continuity equation as

$$v_s = \frac{\dot{h}}{h} \left(x_s + \frac{(x_{s+1} - x_s)}{2} \right) \quad (7)$$

A commonly used relation between shear stress and the slip velocity is a hydrodynamic power-law model

$$\tau = -\lambda \left(\frac{v_s}{v_0} \right)^{m-1} v_s \quad (8)$$

with a power-law coefficient m , a hydrodynamic friction coefficient λ and an arbitrary reference velocity v_0 to normalize the power-law term [11, 12]. The characterization of these parameters is notoriously difficult and subjected to strong uncertainties, as they can be only obtained by large scale in-mold rheology. Due to high pressures, uncertainties of pressure sensors and deviations from the assumed ideal flow kinematics, evaluation of friction stress parameters is ambiguous. To mitigate some of uncertainty, the evaluation considers only pressure differences $p_s - p_{s+1} > 5$ bar due to the low precision of sensors. Nonetheless, the choice of parameters given in Table 3, which are typical values according to relevant literature, give a reasonable parameterization of shear stress featuring a power law behavior (see Figure 5). The linear trend towards higher friction stresses with higher slip velocities in the double logarithmic diagram in Figure 5 supports the application of a power-law friction model.

Property	Value
Reference velocity v_0	1 mm s ⁻¹
Power-law coefficient m	0.6
Hydrodynamic friction coefficient λ	3.0 MN s m ⁻³

Table 3: Mold friction parameters

2.3.2. Compaction behavior

The SMC under investigation shows compressible behavior, as previously reported in [12]. The compressibility in recent high-performance SMCs is caused by their high initial pore content [34]. Specimens with 100% mold coverage are consolidated under typical SMC process conditions to determine an equation of state that relates pressure and volumetric strain. Automated cutting of SMC sheets ensures an accurate initial mold

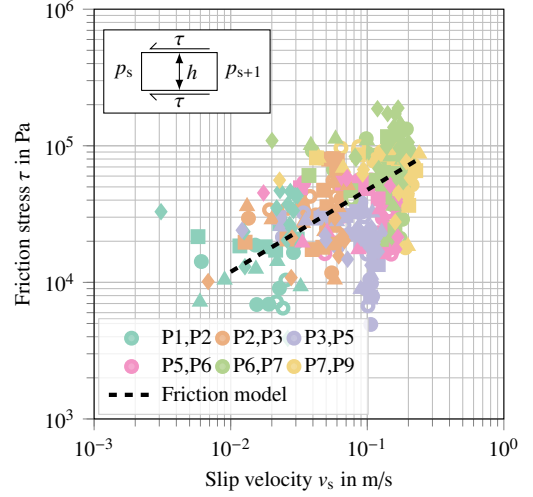


Figure 5: Friction stress evaluation. Colors refer to the first sensor of each sensor pair according to Figure 4. The marker styles differentiate individual molding trials with 75% initial mold coverage each. The hydrodynamic power-law friction model with parameters from Table 3 is indicated by the dashed black line.

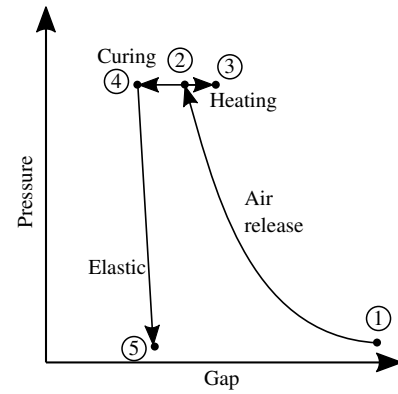


Figure 6: Schematic relation between pressure and mold gap for compression. 1) First contact between mold and SMC stack. 2) The maximum compression force is reached. 3) The maximum thermal extension is reached. 4) The part is fully cured. 5) The part is demolded.

coverage and compression data (force, mold displacements) is recorded during the trials.

The expected behavior is illustrated in the schematic in Figure 6: Upon first contact, the bulk material offers small resistance to compression, as trapped air is compressed and released. The resistance increases, as an increasing amount of air pockets is closed and air escapes until the maximum compression force is reached. At this constant compression force, the material first expands due to heating and consequently shrinks due to cross linking of the thermosetting polymer. Finally, the cured part expands elastically as the compression force is relaxed and the mold opens. The final recorded gap is the part thickness.

Only the region of the rising flank between point 1 and 2 is of interest for the compression molding simulation here. Therefore, these points are extracted and plotted over the Hencky strain $E = \ln(h/h_0)$ in Figure 7. The resulting high compress-

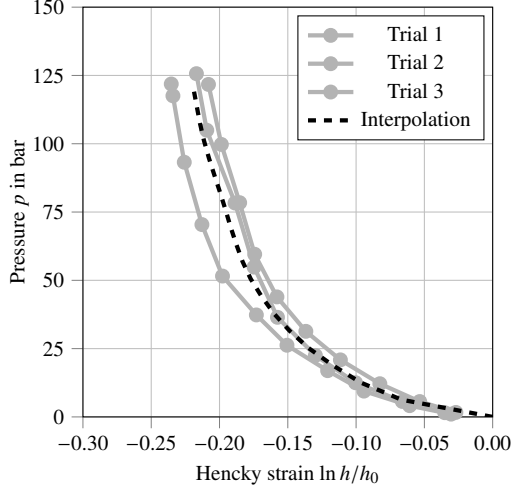


Figure 7: Compaction behavior of the UPPH-GF SMC. The recorded data is corrected with the stiffness of the mold and press, which is determined from an empty stroke. The corrected data is shown in light colors. The rising flank is interpolated and used as tabulated data to describe the relation between Hencky strain and pressure.

ibility is comparable to other structural SMCs reported in recent literature [13]. An averaged relation between strain and pressure is obtained by averaging the strains at various pressure levels. This tabulated data is then used to interpolate the equation of state $p(E)$ in subsequent simulations.

3. Models

3.1. Governing equations

The governing equations for the SMC deformation in a domain Ω are the conservation of mass, conservation of momentum and conservation of internal energy

$$\frac{\partial \rho}{\partial t} + \nabla \cdot (\rho \mathbf{v}) = 0 \quad \mathbf{x} \in \Omega \quad (9)$$

$$\frac{\partial (\rho \mathbf{v})}{\partial t} + \nabla \cdot ((\rho \mathbf{v}) \otimes \mathbf{v}) = \nabla \cdot \boldsymbol{\sigma} + \mathbf{f} \quad \mathbf{x} \in \Omega \quad (10)$$

$$\frac{\partial (\rho c_p T)}{\partial t} + \nabla \cdot ((\rho c_p T) \mathbf{v}) = \nabla \cdot \mathbf{h} \quad \mathbf{x} \in \Omega \quad (11)$$

with mass density $\rho \in \mathcal{R}$, fluid velocity $\mathbf{v} \in \mathcal{R}^3$, Cauchy stress $\boldsymbol{\sigma} \in \mathcal{R}^{3 \times 3}$, symmetric strain rate $\mathbf{D} \in \mathcal{R}^{3 \times 3}$, a body force field $\mathbf{f} \in \mathcal{R}^3$, temperature $T \in \mathcal{R}$ and the non-convective heat flux $\mathbf{h} \in \mathcal{R}^3$. The specific heat capacity c_p is assumed to be constant and gravity as well as heating by viscous dissipation are neglected, as their influence on results is expected to be small. The boundary of Ω is divided into the mold contact area $\partial\Omega_M$ and the free flow front $\partial\Omega_F$ with boundary conditions

$$\mathbf{v} \cdot \mathbf{n} = v_M \quad \boldsymbol{\sigma} \cdot \mathbf{n} = \boldsymbol{\tau} \quad \mathbf{h} \cdot \mathbf{n} = -k(T_M - T) \quad \mathbf{x} \in \partial\Omega_M \quad (12)$$

$$\boldsymbol{\sigma} \cdot \mathbf{n} = \mathbf{0} \quad \mathbf{h} \cdot \mathbf{n} = 0 \quad \mathbf{x} \in \partial\Omega_F, \quad (13)$$

where \mathbf{n} denotes the normal of a boundary surface and v_M denotes the mold velocity ($v_M = 0$ at bottom, $v_M = \dot{h}$ at top).

In this work, these equations are solved at mesoscale utilizing a three-dimensional model simulating the motion of individual fiber bundles and at macroscale using a reduced one-dimensional model for the elongational flow in a press rheometer.

3.2. Mesoscale direct bundle simulation

3.2.1. Overview

The basic idea of the Direct Bundle Simulation is the description of fiber bundles by chains of 1D truss elements that interact with matrix material during the compression molding process. The trusses are subjected to hydrodynamic interaction forces by the matrix fluid, while the fluid experiences opposing forces. The direct simulation of bundles eliminates the need for fiber orientation models, closure approximations, modeling of long-range hydrodynamic interactions and improves the accuracy of simulated fiber architecture in regions, where scale-separation does not apply [29].

An operator splitting scheme is used to solve the governing Equations (9), (10) and (11) in a Coupled Eulerian-Lagrangian simulation framework implemented in SIMULIA Abaqus. The method assigns an element volume fraction of material to each element and reconstructs the material surface that may interact with Lagrangian bodies representing molds at $\partial\Omega_M$ [35] or form a free surface at $\partial\Omega_F$. The interaction between bundles and matrix is integrated via several user subroutines to the simulation, which define a body force field \mathbf{f} based on the hydrodynamic interactions with suspended truss elements.

3.2.2. Hydrodynamic interactions between bundles and matrix

The motion of fiber bundle segments is governed by hydrodynamic forces acting between fluid and bundle segment as well as short range interactions with other bundles. The hydrodynamic force on a bundle segment j is computed as

$$\mathbf{F}_j = 6\pi\eta R (k_d \Delta \mathbf{v}_j + k_l \|\Delta \mathbf{v}_j\| \mathbf{q}) \quad (14)$$

with matrix viscosity η , bundle radius R and a direction \mathbf{q} orthogonal to the bundle axis. The factors k_d and k_l are coefficients determined from micro-simulations and depend on segment aspect ratio as well as orientation of the bundle [29]. The matrix viscosity η depends on the local temperature and shear rate of the neighboring fluid as defined in equation (4), but is assumed locally constant at microscale (i.e. the coefficients k_d and k_l remain the same as for the Newtonian case).

The computation of the relative velocity $\Delta \mathbf{v}$ requires knowledge of the neighborhood relation between bundle segments and surrounding fluid cells. The formal task is finding the set

$$\mathcal{S}_j = \{i \in \mathcal{E} \mid \|x_i - x_j\| < L\} \quad (15)$$

for each bundle center x_j , where \mathcal{E} is the set of fluid cells defined by unique integer labels, L is the search radius (typically equal to segment length) and $x_i, x_j \in \Omega$. A simplistic approach for this task is searching all neighbors for each bundle segment during each time step. This original formulation used in [29] leads to a quadratic search complexity $O(n^2)$ and slows down

larger simulations quite significantly. To address this major bottleneck, the neighborhood search now utilizes a binary space partitioning tree (kd-tree). This improves the search complexity to $O(n \log n)$ and is implemented with the highly optimized library KDTree2 [36].

The relative velocity is then determined from the neighbors as

$$\Delta \mathbf{v}_j = \sum_{i \in S_j} \frac{w_{ij}}{W_j} (\mathbf{v}_i - \mathbf{v}_j) \quad (16)$$

with Gaussian weighting factors w_{ij} and $W_j = \sum_{i \in S} w_{ij}$. The weighted hydrodynamic forces are used to apply an opposed body force field \mathbf{f} on the fluid phase by summing up the contribution of each bundle j in fluid element i

$$\mathbf{f}_{ij} = -\frac{1}{V_i} \frac{w_{ij}}{W_j} \mathbf{F}_j \quad (17)$$

with the volume V_i of the i -th element.

Fiber bundles in close proximity experience normal forces and lubrication forces due to the thin sheared fluid layer between them. Friction forces and lubrication moments are typically neglected for bundled suspensions [37, 20]. While normal penetration of fiber bundles is prohibited by a linear contact stiffness, the tangential contact stresses are defined as

$$\boldsymbol{\sigma}_c = -\eta \frac{d_a^2}{|\sin \phi|} \frac{\Delta \mathbf{v}_t}{\bar{\eta}(g)A}, g > 0 \quad (18)$$

with bundle width d_a , contact angle ϕ , relative tangential velocity $\Delta \mathbf{v}_t$, contact area A as well as the relation between physical gap g and the effective sheared gap $\bar{\eta}(g)$ [31]. However, the tangential stresses are unbound and therefore can lead to infeasible small time steps. Therefore, the maximum tangential stress is bound to an upper limit such that it does not negatively affect the time step.

The presence of fiber bundles and the body force field \mathbf{f} renders a generally anisotropic flow behavior of the SMC. It has been proven to agree with analytical solutions in simple compression for Newtonian matrix and absence of friction [31].

3.2.3. Application to a press rheometer

As the flow in a press rheometer is mostly elongational with no changes in the perpendicular direction, only a 50 mm wide strip of the tool is modeled. The tool itself is represented by isothermal rigid bodies with a temperature of 145 °C. The rigid bodies are in contact with the SMC surface employing a penalty term to prevent penetration, a friction term implementing Equation (8) and a thermal heat flux according to Equation (12). The cavity is represented by an Eulerian domain, in which the initially filled subset Ω_0 representing the SMC stack is defined with an element volume fraction field. In reality, the stack is in contact with the bottom mold for approximately 10 s until the upper mold arrives at the top of the stack. This yields to an unsymmetrical initial heat distribution, which is introduced to the simulation by solving the heat transfer process separately and applying the solution as initial temperature field. Fiber bundles are generated within the stack Ω_0 randomly from a uniform planar isotropic orientation distribution until the desired

volume fraction of 23% is reached. The bundles are 25 mm long, are meshed with 2.5 mm long truss elements and have a cross sectional area of 0.03 mm². The truss sections are elastic with $E = 72$ GPa. Bundle elements extending outside the stack domain are removed, such that shorter fibers are present close to the edges of a stack just like in the physical process. The initial setup is shown in Figure 8.

A global mass scaling factor of 10^4 is applied to reduce computation time of the explicit time stepping procedure and it was verified that the kinetic energy due to this modification is small compared to the total work energy of compression.

3.3. A one-dimensional macroscale reference model

3.3.1. Overview

The mesoscale simulation model is applicable to arbitrary three-dimensional flows and has previously proven to provide accurate predictions of the fiber bundle architecture [29, 30]. However, its evaluation is computationally expensive and efficient macroscale models remain relevant for the application in simple planar SMC flows. Hence, a macroscale reference model for the elongational flow in a press rheometer is formulated as a one-dimensional model for comparison with the high fidelity mesoscale model.

The macroscale reference model uses fiber orientation tensors to describe the orientation state as a stochastic moment of the fiber orientation distribution function $\psi : \mathcal{K}^2 \rightarrow \mathcal{R}_{\geq 0}$, where ψ describes the likelihood to find a fiber in a given direction $\mathbf{p} \in \mathcal{K}^2$. The second and fourth order fiber orientation tensors are defined here as

$$\mathbf{A} = \int_{\mathcal{K}^2} \psi(\mathbf{p}) \mathbf{p} \otimes \mathbf{p} d\mathbf{a} \in \mathcal{R}^{3 \times 3} \quad (19)$$

$$\mathbb{A} = \int_{\mathcal{K}^2} \psi(\mathbf{p}) \mathbf{p} \otimes \mathbf{p} \otimes \mathbf{p} \otimes \mathbf{p} d\mathbf{a} \in \mathcal{R}^{3 \times 3 \times 3 \times 3}, \quad (20)$$

where $\int_{\mathcal{K}^2} \bullet d\mathbf{a}$ denotes an integration over a unit sphere \mathcal{K}^2 . Jeffery's equation [15] can be expressed in terms of fiber orientation tensors as

$$\dot{\mathbf{A}} = \mathbf{W} \cdot \mathbf{A} + \mathbf{A} \cdot \mathbf{W} + \xi (\mathbf{D} \cdot \mathbf{A} + \mathbf{A} \cdot \mathbf{D} - 2\mathbb{A} : \mathbf{D}) \quad (21)$$

with a shape factor $\xi \in [0, 1]$ and with $(\dot{\bullet})$ denoting a material derivative. The tensors $\mathbf{D} \in \mathcal{R}^{3 \times 3}$ and $\mathbf{W} \in \mathcal{R}^{3 \times 3}$ are the symmetric strain rate tensor and vorticity tensor, respectively.

The following simplifications are introduced for the one-dimensional reference model:

- There is no velocity gradient perpendicular to the flow ($D_{yy} = 0$).
- The velocity gradient in compression direction is prescribed by the mold closing speed ($D_{zz} = \frac{\dot{h}}{h}$).
- The material undergoes a perfect plug-flow without shear ($D_{ij} = 0, i \neq j$ and $\mathbf{W} \equiv \mathbf{0}$).
- The fiber orientation state is planar ($A_{xz} = A_{yz} = A_{zz} = 0$).
- The fibers are long and slender ($\xi = 1$).

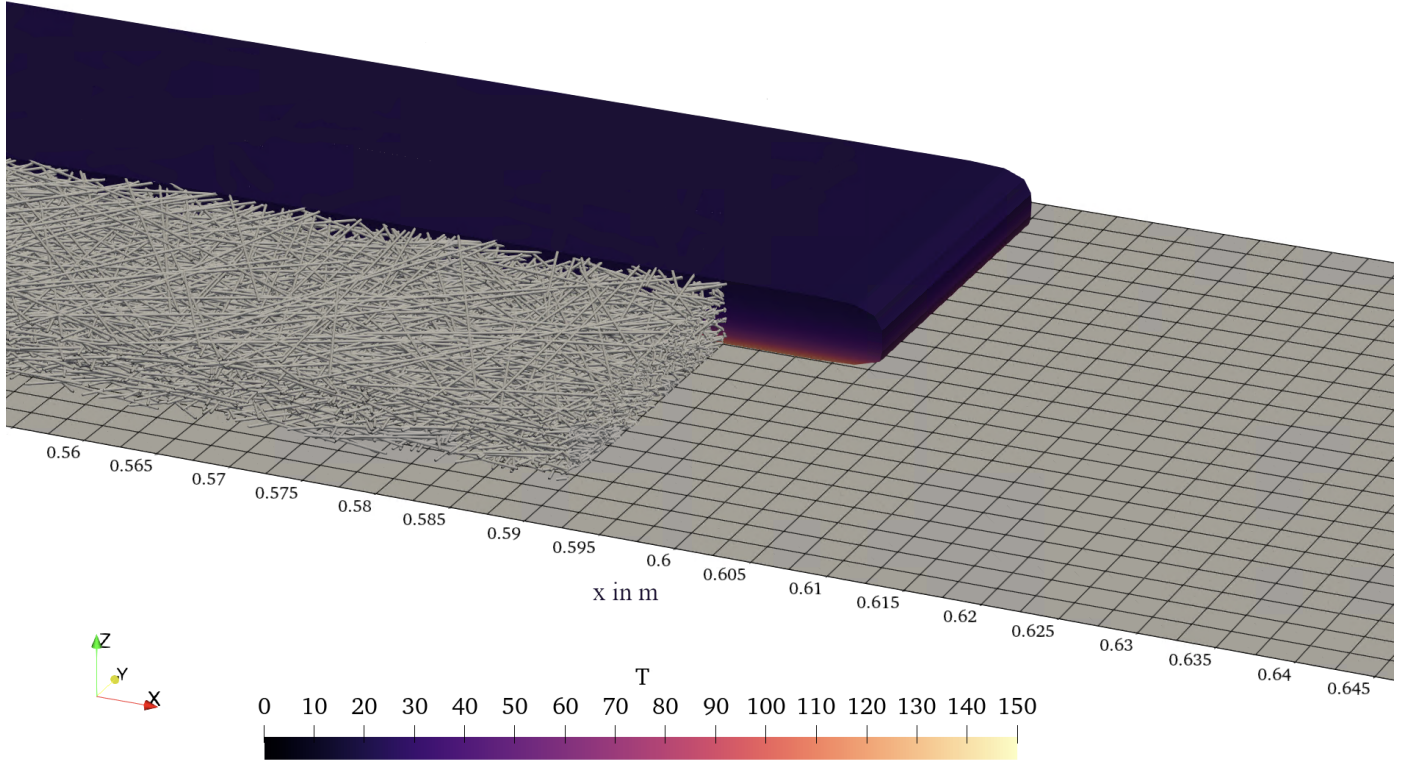


Figure 8: Initial setup of the mesoscale simulation model. The upper mold is not shown and cuts are applied to the filled Eulerian domain as well as the bundle structure for visualization purposes.

- An affine map $m : \Omega_{1D} \rightarrow \Omega_{1D}^*$ transforms the local coordinate $x \in [0, X_{\max}]$ to a stretched coordinate $x^* = m(x) = x/X(t) \in [0, 1]$. Here, $X \in [X_0, X_{\max}]$ denotes the flow front position. Applying chain rule, the spatial gradient becomes $\frac{\partial \bullet}{\partial x} = \frac{\partial \bullet}{\partial x^*} \frac{\partial x^*}{\partial x} = \frac{1}{X} \frac{\partial \bullet}{\partial x^*}$.
- The solution variables are thickness averaged values depending only on time t and one-dimensional position x^* .

3.3.2. Average temperature

The temperature between two closing plates with constant closing speeds and ideal heat transfer at the mold surfaces (Dirichlet boundaries) has been reported in literature [38, 39]. Averaging this result for the temperature distribution over the thickness yields

$$\bar{T}(t) = T_M + (T_M - T_0) \left[\frac{4}{\pi^2} \sum_{q=1}^{\infty} \frac{\cos(q\pi - 1)}{q^2} \exp\left(\frac{-q^2 \pi^2 \kappa t}{h_0 h \rho c_p}\right) \right] \quad (22)$$

as an approximation of the average temperature in the SMC material. This explicit formulation depends only on time and can be evaluated separately.

3.3.3. Constitutive model

The SMC is modeled as compressible anisotropic viscous material. Hence, the stress is computed as

$$\boldsymbol{\sigma} = -p(\rho)\mathbf{I} + \mathbb{V} : \mathbf{D}', \quad (23)$$

where $p(\rho)$ is evaluated from the tabulated data shown in Figure 7, \mathbf{I} denotes the identity tensor and $\mathbf{D}' = \mathbb{P}_2 \mathbf{D}$ denotes the deviatoric strain rate tensor.¹ The anisotropic viscosity tensor is given by

$$\mathbb{V} = 2\eta \mathbb{P}_2 + \eta_2 \left(\mathbb{A} - \frac{1}{3} \mathbf{I} \otimes \mathbf{A} \right) \quad (24)$$

with

$$\eta_2 = \frac{4f r_p^2}{3 [\ln(1/f) + \ln \ln(1/f) + C]} \eta \quad (25)$$

for a semi-dilute suspension of rods with fiber volume fraction f , fiber aspect ratio r_p and a constant parameter $C = 0.1585$ [40]. The fourth-order orientation tensor \mathbb{A} is computed with an IBOF closure approximation [41]. Assuming planar orientation, the absence of strain perpendicular to the flow and perfect plug-flow behavior, the expression reduces to only four

¹The identity tensor on symmetric fourth order tensors may be decomposed in a spherical and deviatoric projector $\mathbb{I}^s = \mathbb{P}_1 + \mathbb{P}_2$. While the spherical projector $\mathbb{P}_1 = \frac{1}{3} \mathbf{I} \otimes \mathbf{I}$ can be used to extract the volumetric part of a second order tensor (such as strain rate tensor \mathbf{D}), the deviatoric projector $\mathbb{P}_2 = \mathbb{I}^s - \mathbb{P}_1$ may be used to obtain the deviatoric part.

non-trivial components

$$V_{xxxx} = \frac{4}{3}\eta + \eta_2 \left(A_{xxxx} - \frac{1}{3}A_{xx} \right) \quad (26)$$

$$V_{zzxx} = -\frac{2}{3}\eta - \frac{1}{3}\eta_2 A_{xx} \quad (27)$$

$$V_{zzzz} = \frac{4}{3}\eta \quad (28)$$

$$V_{xxzz} = -\frac{2}{3}\eta \quad (29)$$

3.3.4. Initial boundary value problem

Introducing the simplifications to the conservation of mass, conservation of momentum and orientation equation results in the system of equations

$$\frac{\dot{\rho}}{\rho} = -\frac{1}{X} \frac{\partial v}{\partial x^*} - \frac{\dot{h}}{h} \quad (30)$$

$$\rho \dot{v} = \frac{1}{X} \frac{\partial}{\partial x^*} (-p(\rho) + V_{xxxx}D_{xx} + V_{xxzz}D_{zz}) - 2\lambda \frac{v}{h} \left(\frac{v}{v_0} \right)^{m-1} \quad (31)$$

$$\dot{A}_{xx} = 2(A_{xx} - A_{xxxx})D_{xx} \quad (32)$$

$$\dot{A}_{yy} = -2A_{yyxx}D_{xx} \quad (33)$$

$$\dot{A}_{xy} = (A_{xy} - 2A_{xyxx})D_{xx}, \quad (34)$$

for the solution variables ρ , v , A_{xx} , A_{yy} and A_{xy} . Initially, the values are $\rho_0 = 1480 \text{ kg m}^{-3}$, $v_0 = 0$, $A_{xx} = 0.5$, $A_{yy} = 0.5$ and $A_{xy} = 0$. The boundary condition for the momentum equation at $x^* = 0$ is $v = 0$ at all times. At $x^* = 1$, the boundary condition changes after complete filling and is given as

$$0 = \begin{cases} -p(\rho) + V_{xxxx}D_{xx} + V_{xxzz}D_{zz}, & \text{if } X < X_{\max} \\ v, & \text{if } X = X_{\max} \end{cases}. \quad (35)$$

All other boundaries are no-flux boundaries.

The initial boundary value problem is solved numerically in MATLAB using the *pdepe* solver with 40 discretization points for x^* and a dynamic time step (see Appendix C for implementation details).

3.4. Press control model

The physical press follows a press profile given as m pairs of tool gap and corresponding closing velocity $((h_0, \dot{h}_0), (h_1, \dot{h}_1), \dots, (h_m, \dot{h}_m))$. Eventually the controller switches to force-control in order to limit stresses on mold and press. A virtual press-controller is used to mimic this behavior as boundary condition during the compression molding simulation. As long as the compression force is below the force at switch-over F_{\max} , the profile is linearly interpolated to obtain the current press velocity. After the switch-over increment l_0 , a simple PI-controller is employed to determine the current velocity

$$\dot{h}_{l+1} = \dot{h}_l + P_p \epsilon_l + P_i \sum_{i=l_0}^l \frac{\epsilon_i}{2} \Delta t \quad (36)$$

from the normalized error

$$\epsilon_i = \frac{F_{\max} - F_i}{F_{\max}} \dot{h}_m. \quad (37)$$

The normalization ensures reliable force-control through a wide range of simulation parameters with constant control parameters $P_p = P_i = 0.5$.

In the specific case of this press rheometer, the press profile is set to a constant closing speed $((h_0 = 10 \text{ mm}, \dot{h}_0 = -1 \text{ mm s}^{-1}), (h_1 = 0 \text{ mm}, \dot{h}_1 = -1 \text{ mm s}^{-1}))$ with a maximum compression force of $F_{\max} = 4400 \text{ kN}$.

4. Results

Figures 9 and 10 illustrate the evolution of compression force, pressures and orientation over compression time for press rheometer compression trials and simulations with 75% and 25% initial mold coverage, respectively. The initial stacks are always aligned to the left of the cavity, as depicted in Figure 4. The median experimental results are plotted with light colored solid lines and light colored areas between the first and third quartile, which were obtained from five trials per configuration. Additionally, mesoscale simulation results are displayed as solid dark lines and one-dimensional simulation results are displayed as dashed dark lines. All these results are aligned such that the time $t = 0$ describes the switch from displacement controlled mold closing to pressure control.

4.1. 75% mold coverage

An initial stack of 75% mold coverage is realized by four sheets with dimensions 600 mm x 450 mm x 4.5 mm. The experimental compression of these stacks leads to repeatable recordings for the total compression force and pressures, i.e. the area between first and third quartile is narrow (see Figure 9 a and b). The pressure sensor readings (see light solid lines in Figure 9 b) are as expected with an increase of pressure from P01 to P09 during the elongational flow. However, the sensors do not immediately converge to the nominal pressure $\bar{p} = 122 \text{ bar}$ after the mold filling is completed at about 1.5 s after reaching maximum compression force.

The mesoscale simulation and the macroscale reference model predict a compression force similar to the experimental recording (see Figure 9 a). The simulated pressure curves feature a bend at $t = 0$ due to the transition to a pressure controlled mold closure. A second bend occurs when the mold is completely filled and pressure sensors converge towards the nominal pressure \bar{p} . The spread between P01 and P09 is larger in the mesoscale simulation than in the macroscale model. Both simulations overestimate the pressure difference between P01 and P02 slightly and underestimate the total time to complete mold filling. A likely cause for both effects is a loss of material through the mold gap at the left side of the tool in the experiments due to the high pressure.

The simulated fiber orientation of the high fidelity mesoscale model gives similar results to the one-dimensional model based on Jeffery's equation (see Figure 9 c). The mesoscale model

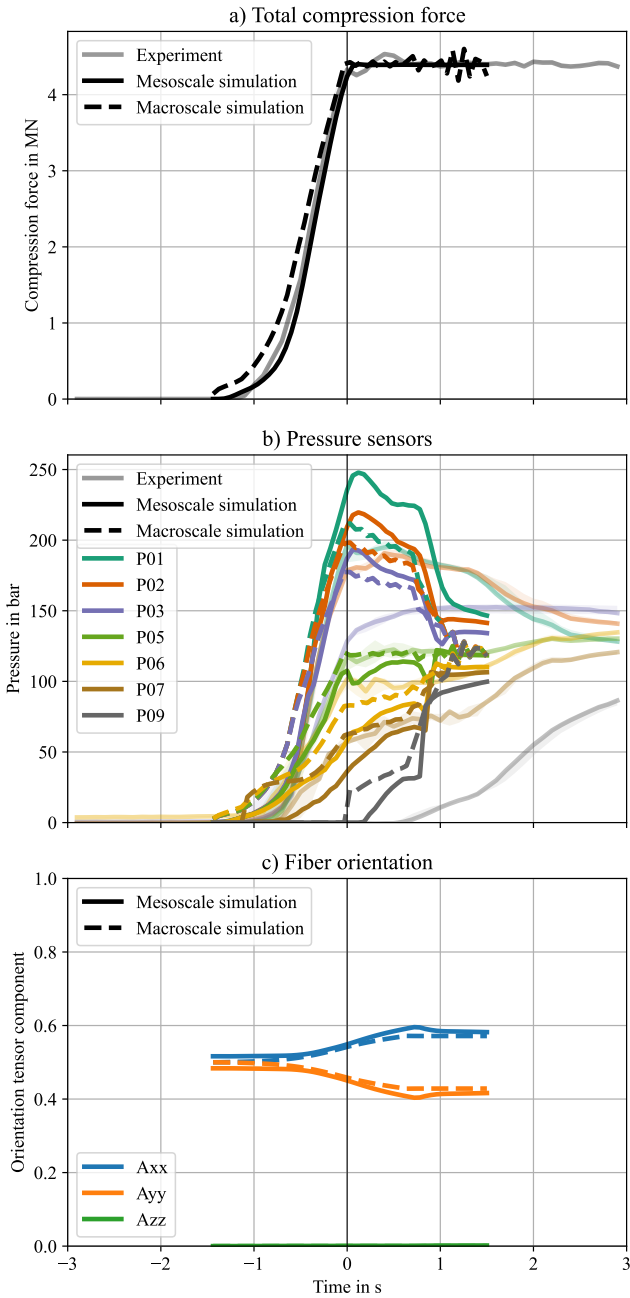


Figure 9: Evolution of process parameters for 75% initial mold coverage with a shared axis for time, where $t = 0$ is the experimental switching point from displacement control to pressure control. The colors and pressure sensor labels in subplot b) refer to the sensor locations indicated in Figure 4.

has a small initial orientation preference towards the flow direction, which is an artifact of the initial stack generation. It predicts a reduction of the orientation preference as soon as the mold is completely filled, because bundles at both ends of the mold are forced to a orientation parallel to the wall by non-local effects [29]. Noticeably, the evaluated A_{zz} component remains negligible, because the 25 mm long fiber bundles are highly constrained between the mold walls, which are located less than 4.5 mm apart. Therefore, the assumption of pla-

nar orientation in the one-dimensional model holds. Further, the bundle architecture deforms without significant through-thickness shear, making the perfect plug-flow assumption of the one-dimensional model applicable in this case.

4.2. 25% mold coverage

Compared to the previous case, experimental results feature a larger uncertainty and the ranking of recorded pressure levels is not as expected. The leftmost sensor P01 records a pressure drop with pressures that are significantly lower than P02 and even P03. An initial stack of 25% mold coverage is realized by nine sheets with dimensions 200 mm x 450 mm x 8.5 mm. This behavior is not correctly reproduced by the simulation models. The computed forces of the macroscale reference model are too large and result in premature switch to the pressure controlled phase and subsequently in an over-prediction of fill time. The mesoscale simulation yields reasonable results at the end of filling, but also fails to predict the severe pressure drop in sensors P01 and P02. A cause for the deviation is possibly a deformation mode that is significantly different from ideal plug-flow. To investigate this deviation from the plug-flow assumption, plaques with a colored central sheet were manufactured. A photo of such a molded plaque is given in Figure 11. While a perfect plug-flow would result in a homogeneously stretched black layer, the photo shows that the black sheet is shifted and not fully stretched along the flow path. Areas outside black region feature compressed fiber bundles with distinct flow marks separating those regions. Figure 12 shows a corresponding top view of predicted positions for fiber bundles, which were initially positioned at the stack center. The simulation shows a lack of black colored fiber bundles from the central sheet at both ends, albeit to a much lower extend than observed experimentally. Even though the mesoscale simulation predicts some shear in the fiber bundle architecture shortly after compression start due to the inhomogeneous temperature (see Figure 13), the extent does not agree with experiments. However, the similar simulated orientation state between both models highlights once again that Jeffery's basic model agrees well with a direct simulation model for highly confined planar flow.

5. Discussion

The results show a reasonable agreement between a one-dimensional macroscale model, a mesoscale model with individual resolved fiber bundles, and experimental results for a thin SMC stack with 75% mold coverage. Unlike a mere comparison of compression forces, the comparison of pressures in the mold allows a more detailed evaluation of contributions to the total compression force by mold friction and viscous elongation. The observed pressure reduction from P01 to P09 is expected and indicates a correct proportion of those contributions in both models.

For a thick stack with a small mold coverage of 25%, the results deviate significantly. A likely reason for this deviation is that the deformation kinematics differ notably from ideal plug-flow conditions. In that case, the one-dimensional reference

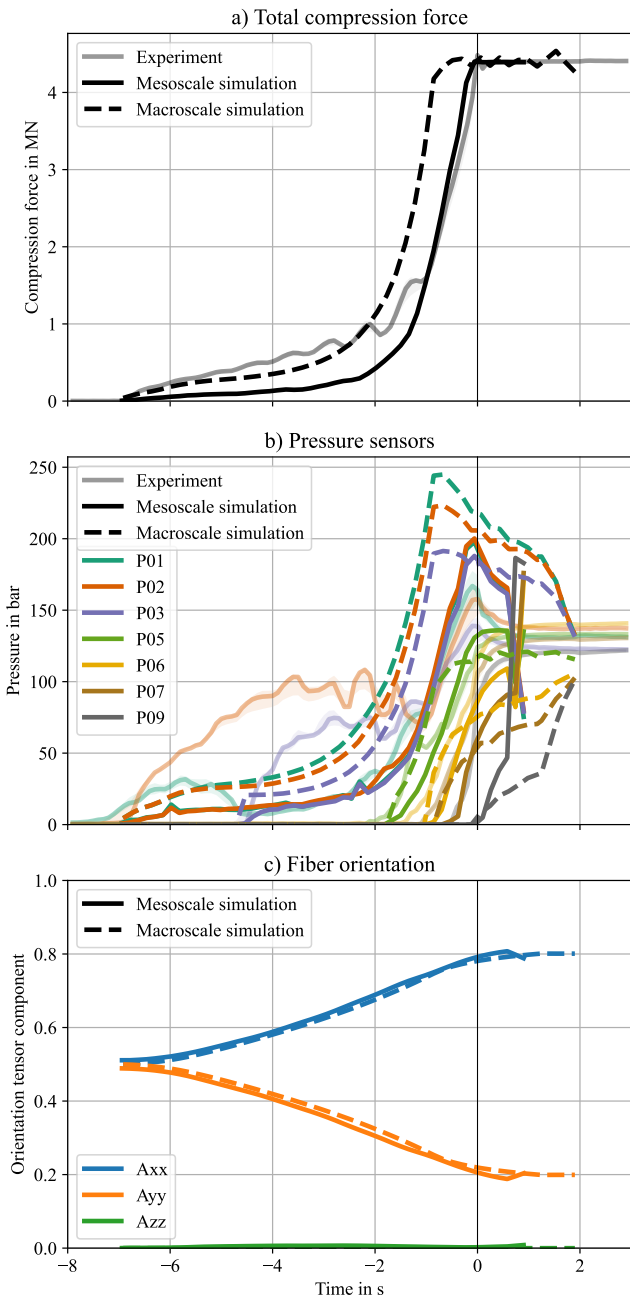


Figure 10: Evolution of process parameters for 25% initial mold coverage with a shared axis for time, where $t = 0$ is the experimental switching point from displacement control to pressure control. The colors and pressure sensor labels in subplot b) refer to the sensor locations indicated in Figure 4.

model cannot predict accurate results, as the entire formulation is based on a plug-flow hypothesis. The mesoscale simulation shows initial shear contributions due to a non-isothermal temperature distribution in the stack and the initial deformation mode shown in Figure 13 agrees well with observations from literature [42]. However, the mesoscale model is also not able to fully explain the unexpected pressure histories, shift of the central sheet and formation of areas with compressed fibers at both ends of the mold.

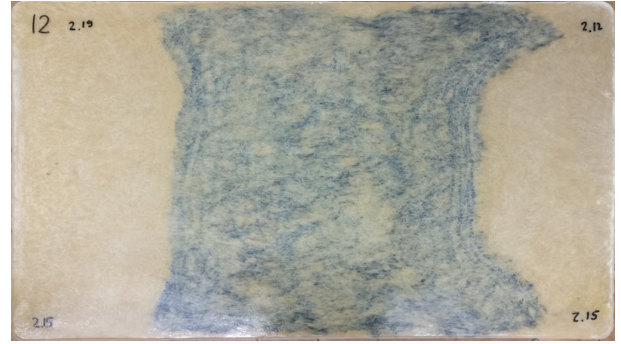


Figure 11: Top view of a molded plaque with a colored sheet at the stack center. The colored sheet has not been stretched over the entire length of the tool (as a plug-flow assumption would suggest), but is transported with relatively low stretch (see Figure 4 for initial sheet placement).

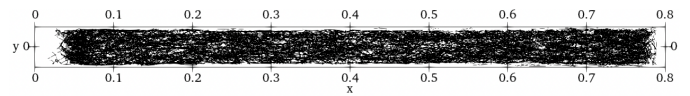


Figure 12: Top view of simulated fiber bundles, which were initially located at the stack center (see Figure 13 for a side view of initial placement). Compared to the experimental results, the simulation predicts significantly more stretch in flow direction.

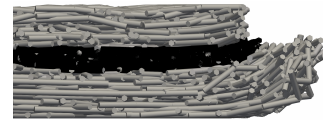


Figure 13: Detail view of the bundle architecture for 25% mold coverage close to the flow front shortly after the start of the compression process. Fiber bundles, that are located initially at the stack center, are colored black.

Possible deformation modes for the investigated SMC are either a *squeeze mechanism*, in which the central sheet is pushed out or a *slide mechanism*, in which the stack is sheared on the hotter lubricated bottom mold (see Figure 14). Both mechanisms would explain the pressure drop of leftmost sensors by an empty region due to the shift of sheets to the right. The

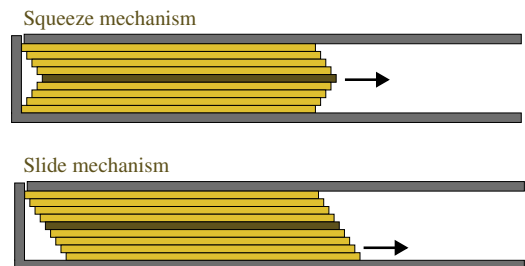


Figure 14: Possible deformation modes.

squeeze mechanism would require a transition to a preferred flow of outer hot layers during the compression process, otherwise Figure 11 would show a concentration of the black colored sheet at one end of the mold. The slide mechanism is deemed more likely and would explain areas with compressed

fiber bundles, as the complete fill of the empty regions requires a compression of the outermost sheets. Areas of compressed and regular fiber bundles have been previously reported for the same material [43].

The flow kinematic and resulting pressures could be caused by a yield stress or by a sticking behavior at the mold surface that has to overcome a threshold before entering a hydrodynamic friction regime. Further development of characterization methods for the friction model considering temperature changes are required in the future. Also, the mesoscale simulation model might benefit from distinguishing individual sheets to represent the stack more accurately. However, this would require a finer numerical resolution and a method to merge sheets, as they are smeared together in more complex flow scenarios.

Additional sources of error in the one-dimensional macroscale model are the application of Shaqfeh and Fredrickson's [40] equations, which are originally intended for semi-dilute suspensions only.

Thermal conductivity κ is measured only transverse to sheets, even though it is actually an anisotropic tensor with different (orientation dependent) in-plane properties. However, the scalar treatment is considered an acceptable simplification, because the heat transfer in this application is dominated by the transverse heat flow and in-plane heat conduction is rather small compared to in-plane convection.

It is remarkable that Jeffery's equation yields results close to a high fidelity direct simulation of individual fiber bundles at mesoscale. Jeffery's model has been improved with diffusion terms that drive the orientation towards a more isotropic state, because random fiber collisions lead to a net motion towards more random orientations [17]. These diffusion terms were developed with a particular focus on short fiber injection molding. In SMC compression molding however, a diffusion term of the form $\dot{A}_D \propto \dot{\gamma}(\mathbf{I} - 3\mathbf{A})$ with $\dot{\gamma} = \sqrt{2\mathbf{D}' : \mathbf{D}'}$ would generate a positive component A_{zz} component. This component is suppressed for long fibers by the narrow gap between molds, as seen in the direct simulations. Hence, Jeffery's basic model seems better suited for planar SMC simulation than its derivations with empirical diffusion terms.

6. Conclusions and Outlook

First, this study reports characterization of key properties for non-isothermal, non-Newtonian compressible behavior of UPPH glass fiber SMC. The thermal properties include transverse heat conductivity and conductance from mold to SMC, which were determined from temperature measurements in an SMC stack. The viscosity of the paste is measured in a plate-plate rheometer and shows typical power-law behavior. The hydrodynamic mold friction is computed from pressure differences in an instrumented press rheometer and shows a power-law behavior as well. The press rheometer is also used to obtain a tabulated expression for the relation between pressure and volumetric compression.

Flow in a press rheometer is then simulated with a high-fidelity mesoscale direct bundle simulation as well as a one-dimensional macroscale reference model utilizing Jeffery's

equation for fiber orientation. For thin SMC stacks with a large mold coverage of 75%, both models are able to reproduce compression force and pressure sensor recordings. In contrast to a comparison of total compression force only, pressure sensor recordings verify that the contributions from mold friction and anisotropic viscous elongation are in right proportions. However, thick stacks of the investigated SMC with small initial mold coverage experience deformations that deviate significantly from ideal plug-flow assumptions. The one-dimensional reference model cannot describe this deformation by design, but even the detailed mesoscale model is not able to fully predict this behavior. To predict a sliding mechanism, the mesoscale model may be enhanced by an advanced temperature dependent friction model with a threshold for slipping or a differentiation between sheets.

For planar SMC flow of thin stacks, Jeffery's equation agrees well with the computed reorientation of the direct mesoscale simulation. The original formulation without additional diffusion terms can be recommended for planar, plug-flow dominated SMC molding, because fibers are constrained by the molds and have only marginal out-of-plane orientation components.

7. Author Contributions

Conceptualization: N.M., A.H., L.K.; methodology: N.M., S.I.; software: N.M.; validation: N.M. and S.I.; investigation: N.M. and S.I.; resources: N.M., F.H. and L.K.; data curation: N.M.; writing—original draft preparation: N.M.; writing—review and editing: N.M., S.I., A.H., F.H., and L.K.; visualization: N.M.; supervision: A.H., F.H. and L.K.;

8. Acknowledgment

The research documented in this manuscript has been funded by the Deutsche Forschungsgemeinschaft (DFG, German Research Foundation), project number 255730231, within the International Research Training Group "Integrated engineering of continuous-discontinuous long fiber reinforced polymer structures" (GRK 2078). The support by the German Research Foundation (DFG) is gratefully acknowledged.

Appendix A. Tabulated compaction behavior

Appendix B. Implementation details of the mesoscale direct bundle simulation

The direct bundle simulation described in Section 3.2 and Meyer et al. [29] is implemented via several user subroutines in a Coupled Eulerian Lagrangian (CEL) framework in SIMULIA Abaqus Explicit. A VUEXTERNALDB subroutine manages the overall workflow, i.e. parsing input files before the analysis, building kd-trees for each step, evaluating a stable time step and performing checks. A VUFIELD subroutine extracts positions and velocities of nodes in each time step and a VUSDFLD subroutine extrapolates the data to the unique Gaussian point of EC3D8RT and T3D2 elements. The viscosity of

Hencky strain	Pressure in MPa
-0.0000	0.0
-0.0770	6.3
-0.1098	12.6
-0.1325	18.9
-0.1496	25.3
-0.1638	31.6
-0.1749	37.9
-0.1840	44.2
-0.1923	50.5
-0.1982	56.8
-0.2029	63.2
-0.2073	69.5
-0.2116	75.8
-0.2167	82.1
-0.2219	88.4
-0.2270	94.7
-0.2317	101.1
-0.2349	107.4
-0.2378	113.7
-0.2407	120.0

Table A.4: Relation between Hencky strain and pressure

the matrix is computed in a VUVISCOSITY subroutine. Finally, a VDLOAD subroutine is used to evaluate equations (14), (16), and (17). Additionally, a VUINTERACTION subroutine is used to implement Equation (18) and a VUAMP subroutine realizes the press controller described in Section 3.4.

The computation time (wall-clock time) for a full solution is up to 73 h at 25% mold coverage (8 s simulated time) on a workstation with a 16-core Intel Xeon E5-2667 v2 @ 3.3 GHz.

Appendix C. Implementation details of the one-dimensional macroscale reference model

The set of equations (30), (31), (32), (33), (34) are reformulated to

$$C \left(x^*, t, \vec{s}, \frac{\partial \vec{s}}{\partial x^*} \right) \frac{\partial \vec{s}}{\partial t} = \frac{\partial}{\partial x^*} \vec{f} \left(x^*, t, \vec{s}, \frac{\partial \vec{s}}{\partial x^*} \right) + \vec{s} \left(x^*, t, \vec{s}, \frac{\partial \vec{s}}{\partial x^*} \right) \quad (\text{C.1})$$

for a solution variable vector $\vec{s} = (\rho, v, A_{xx}, A_{yy}, A_{xy})^\top$. The coupling matrix is defined as

$$C = \text{diag} \left(\frac{1}{\rho}, \rho, 1, 1, 1 \right), \quad (\text{C.2})$$

the flux is given by

$$\vec{f} = \frac{1}{X} \begin{pmatrix} -v \\ -p(\rho) + V_{xxxx} \frac{1}{X} \frac{\partial v}{\partial x^*} + V_{xxxx} \frac{h}{h} \\ 0 \\ 0 \\ 0 \end{pmatrix}, \quad (\text{C.3})$$

and the source term is given by

$$\vec{s} = \begin{pmatrix} -\frac{h}{h} \\ -2\lambda \frac{v}{h} \left(\frac{v}{v_0} \right)^{m-1} \\ 2(A_{xx} - A_{xxxx}) \frac{1}{X} \frac{\partial v}{\partial x^*} \\ -2A_{yyxx} \frac{1}{X} \frac{\partial v}{\partial x^*} \\ (A_{xy} - A_{xyxx}) \frac{1}{X} \frac{\partial v}{\partial x^*} \end{pmatrix}. \quad (\text{C.4})$$

During time integration, the flow front is updated according to

$$X^{l+1} = X^l + v^l(x^* = 1) \Delta t \quad (\text{C.5})$$

with l denoting the current time step index. The pressures are evaluates as

$$\sigma_{zz} = -p(\rho) + V_{zzxx} \frac{1}{X} \frac{\partial v}{\partial x^*} + V_{zzzz} \frac{h}{h} \quad (\text{C.6})$$

and integrated to compute the total compression force

$$F = W \int_{x^*=0}^X \sigma_{zz}(\tilde{x}) d\tilde{x}. \quad (\text{C.7})$$

The computation time (wall-clock time) for a full solution is up to 3.5 min at 25% mold coverage (8 s simulated time) on a desktop computer with a 4-core Intel Core i7-3770 @ 3.4 GHz.

References

- [1] R. J. Silva-Nieto, B. C. Fisher, A. W. Birley, Predicting mold flow for unsaturated polyester resin sheet molding compounds, *Polymer Composites* 1 (1980) 14–23. doi:10.1002/pc.750010105.
- [2] C. L. Tucker, F. Folgar, A Model of Compression Mold Filling, *Polymer Engineering and Science* 23 (1983) 69–73. doi:10.1002/pen.760230204.
- [3] M. R. Barone, D. A. Caulk, A Model for the Flow of a Chopped Fiber Reinforced Polymer Compound in Compression Molding, *Journal of Applied Mechanics* 53 (1986) 361–371. doi:10.1115/1.3171765.
- [4] J. Görthofer, N. Meyer, T. D. Pallicity, L. Schöttl, A. Trauth, M. Schemmann, M. Hohberg, P. Pinter, P. Elsner, F. Henning, A. N. Hrymak, T. Seelig, K. Weidenmann, L. Kärger, T. Böhlke, Virtual process chain of sheet molding compound: Development, validation and perspectives, *Composites Part B: Engineering* 169 (2019) 133–147. doi:10.1016/j.compositesb.2019.04.001.
- [5] V. Romanenko, M. Duhovic, D. Schommer, J. Hausmann, J. Eschl, Advanced process simulation of compression molded carbon fiber sheet molding compound (C-SMC) parts in automotive series applications, *Composites Part A: Applied Science and Manufacturing* 157 (2022) 106924. doi:10.1016/j.compositesa.2022.106924.
- [6] C.-C. Lee, F. Folgar, C. L. Tucker, Simulation of Compression Molding for Fiber-Reinforced Thermosetting Polymers, *Journal of Engineering for Industry* 106 (1984) 114–125. doi:10.1115/1.3185921.
- [7] T. A. Osswald, C. L. Tucker, A boundary element simulation of compression mold filling, *Polymer Engineering and Science* 28 (1988) 413–420. doi:10.1002/pen.760280703.
- [8] T. A. Osswald, C. L. Tucker, Compression Mold Filling Simulation for Non-Planar Parts, *International Polymer Processing* 5 (1990) 79–87. doi:10.3139/217.900079.
- [9] L. M. Abrams, J. M. Castro, Predicting molding forces during sheet molding compound (SMC) compression molding. I: Model development, *Polymer Composites* 24 (2003) 291–303. doi:10.1002/pc.10029.
- [10] P. J. J. Dumont, L. Orgéas, S. Le Corre, D. Favier, Anisotropic viscoelastic behavior of sheet molding compounds (SMC) during compression molding, *International Journal of Plasticity* 19 (2003) 625–646. doi:10.1016/S0749-6419(01)00077-8.

- [11] P. J. J. Dumont, J.-P. Vassal, L. Orgéas, V. Michaud, D. Favier, J.-A. E. Månson, Processing, characterisation and rheology of transparent concentrated fibre-bundle suspensions, *Rheologica Acta* 46 (2007) 639–651. doi:10.1007/s00397-006-0153-8.
- [12] M. Hohberg, L. Kärger, F. Henning, A. N. Hrymak, Rheological measurements and rheological shell model considering the compressible behavior of long fiber reinforced sheet molding compound (SMC), *Composites Part A: Applied Science and Manufacturing* 95 (2017) 110–117. doi:10.1016/j.compositesa.2017.01.006.
- [13] D. Ferré-Sentis, P. Dumont, L. Orgéas, F. Martoia, M. Sager, Rheological response of compressible SMCs under various deformation kinematics: Experimental aspects and simple modelling approach, *Composites Part A: Applied Science and Manufacturing* 154 (2022) 106774. doi:10.1016/j.compositesa.2021.106774.
- [14] G. Alnersson, M. W. Tahir, A.-L. Ljung, T. S. Lundström, Review of the Numerical Modeling of Compression Molding of Sheet Molding Compound, *Processes* 8 (2020) 179–190. doi:10.3390/pr8020179.
- [15] G. B. Jeffery, The motion of ellipsoidal particles immersed in a viscous fluid, *Proceedings of the Royal Society of London. Series A, Containing Papers of a Mathematical and Physical Character* 102 (1922) 161–179. doi:10.1098/rspa.1922.0078.
- [16] S. G. Advani, C. L. Tucker, The Use of Tensors to Describe and Predict Fiber Orientation in Short Fiber Composites, *Journal of Rheology* 31 (1987) 751–784. doi:10.1122/1.549945.
- [17] F. Folgar, C. L. Tucker, Orientation Behavior of Fibers in Concentrated Suspensions, *Journal of Reinforced Plastics and Composites* 3 (1984) 98–119. doi:10.1177/073168448400300201.
- [18] J. Wang, J. F. O’Gara, C. L. Tucker, An objective model for slow orientation kinetics in concentrated fiber suspensions: Theory and rheological evidence, *Journal of Rheology* 52 (2008) 1179–1200. doi:10.1122/1.2946437.
- [19] J. H. Phelps, C. L. Tucker, An anisotropic rotary diffusion model for fiber orientation in short- and long-fiber thermoplastics, *Journal of Non-Newtonian Fluid Mechanics* 156 (2009) 165–176. doi:10.1016/j.jnnfm.2008.08.002.
- [20] S. Le Corre, P. J. J. Dumont, L. Orgéas, D. Favier, Rheology of highly concentrated planar fiber suspensions, *Journal of Rheology* 49 (2005) 1029–1058. doi:10.1122/1.1993594.
- [21] P. J. J. Dumont, S. Le Corre, L. Orgéas, D. Favier, A numerical analysis of the evolution of bundle orientation in concentrated fibre-bundle suspensions, *Journal of Non-Newtonian Fluid Mechanics* 160 (2009) 76–92. doi:10.1016/j.jnnfm.2009.03.001.
- [22] O. Guiraud, L. Orgéas, P. J. J. Dumont, S. Rolland du Roscoat, Microstructure and deformation micromechanisms of concentrated fiber bundle suspensions: An analysis combining x-ray microtomography and pull-out tests, *Journal of Rheology* 56 (2012) 593–623. doi:10.1122/1.3698185.
- [23] N. Meyer, O. Saburow, M. Hohberg, A. N. Hrymak, F. Henning, L. Kärger, Parameter Identification of Fiber Orientation Models Based on Direct Fiber Simulation with Smoothed Particle Hydrodynamics, *Journal of Composites Science* 4 (2020) 77–96. doi:10.3390/jcs4020077.
- [24] A. Londoño-Hurtado, J. P. Hernandez-Ortiz, T. Osswald, Mechanism of fiber–matrix separation in ribbed compression molded parts, *Polymer Composites* 28 (2007) 451–457. doi:10.1002/pc.20295.
- [25] C. Kuhn, I. Walter, O. Täger, T. Osswald, Simulative Prediction of Fiber-Matrix Separation in Rib Filling During Compression Molding Using a Direct Fiber Simulation, *Journal of Composites Science* 2 (2017) 2–12. doi:10.3390/jcs2010002.
- [26] P. J. J. Dumont, L. Orgéas, D. Favier, P. Pizette, C. Venet, Compression moulding of SMC: In situ experiments, modelling and simulation, *Composites Part A: Applied Science and Manufacturing* 38 (2007) 353–368. doi:10.1016/j.compositesa.2006.03.010.
- [27] T.-H. Le, P. J. J. Dumont, L. Orgéas, D. Favier, L. Salvo, E. Boller, X-ray phase contrast microtomography for the analysis of the fibrous microstructure of SMC composites, *Composites Part A: Applied Science and Manufacturing* 39 (2008) 91–103. doi:10.1016/j.compositesa.2007.08.027.
- [28] A. Motaghi, A. N. Hrymak, Microstructure characterization in direct sheet molding compound, *Polymer Composites* 40 (2019) E69–E77. doi:10.1002/pc.24495.
- [29] N. Meyer, L. Schöttl, L. Bretz, A. N. Hrymak, L. Kärger, Direct Bundle Simulation approach for the compression molding process of Sheet Molding Compound, *Composites Part A: Applied Science and Manufacturing* 132 (2020) 105809. doi:10.1016/j.compositesa.2020.105809.
- [30] F. Rothenhäusler, N. Meyer, S. Wehler, M. Hohberg, M. Gude, F. Henning, L. Kärger, Experimental and Numerical Analysis of SMC Compression Molding in Confined Regions—A Comparison of Simulation Approaches, *Journal of Composites Science* 6 (2022) 68. doi:10.3390/jcs6030068.
- [31] N. Meyer, A. Hrymak, L. Kärger, Modeling Short-Range Interactions in Concentrated Newtonian Fiber Bundle Suspensions, *International Polymer Processing* 36 (2021) 255–263. doi:10.1515/ipp-2020-4051.
- [32] D. Bücheler, F. Henning, Hybrid resin improves position and alignment of continuously reinforced prepreg during compression co-molding with sheet molding compound, in: *Proceedings of the 17th European Conference on Composite Materials, Munich, Germany, 2016*, pp. 1–5.
- [33] F. K. Schwab, C. Dennison, Reaction and characterisation of a two-stage thermoset using molecular dynamics, *Polymer Chemistry* 10 (2019) 4413–4427. doi:10.1039/c9py00521h.
- [34] D. Ferré Sentis, L. Orgéas, P. J. J. Dumont, S. Rolland du Roscoat, M. Sager, P. Latil, 3D in situ observations of the compressibility and pore transport in Sheet Moulding Compounds during the early stages of compression moulding, *Composites Part A: Applied Science and Manufacturing* 92 (2017) 51–61. doi:10.1016/j.compositesa.2016.10.031.
- [35] D. J. Benson, S. Okazawa, Contact in a multi-material Eulerian finite element formulation, *Computer Methods in Applied Mechanics and Engineering* 193 (2004) 4277–4298. doi:10.1016/j.cma.2003.12.061.
- [36] M. B. Kennel, KDTREE 2: Fortran 95 and C++ software to efficiently search for near neighbors in a multi-dimensional Euclidean space, 2004. URL: <http://arxiv.org/abs/physics/0408067>.
- [37] C. Servais, A. Luciani, J.-A. E. Månson, Fiber–fiber interaction in concentrated suspensions: Dispersed fiber bundles, *Journal of Rheology* 43 (1999) 1005–1018. doi:10.1122/1.551015.
- [38] L. J. Lee, L. F. Marker, R. M. Griffith, The Rheology and Mold Flow of Polyester Sheet Molding Compound, *Polymer Composites* 2 (1981) 209–218. doi:10.1002/pc.750020412.
- [39] J. M. Castro, G. Tomlinson, Predicting molding forces in SMC compression molding, *Polymer Engineering and Science* 30 (1990) 1568–1573. doi:10.1002/pen.760302403.
- [40] E. S. G. Shaqfeh, G. H. Fredrickson, The hydrodynamic stress in a suspension of rods, *Physics of Fluids A: Fluid Dynamics* 2 (1990) 7–24. doi:10.1063/1.857683.
- [41] D. H. Chung, T. H. Kwon, Invariant-based optimal fitting closure approximation for the numerical prediction of flow-induced fiber orientation, *Journal of Rheology* 46 (2002) 169–194. doi:10.1122/1.1423312.
- [42] P. T. Odenberger, H. M. Andersson, T. S. Lundström, Experimental flow-front visualisation in compression moulding of SMC, *Composites Part A: Applied Science and Manufacturing* 35 (2004) 1125–1134. doi:10.1016/j.compositesa.2004.03.019.
- [43] M. Schemmann, S. Gajek, T. Böhlke, Biaxial Tensile Tests and Microstructure-Based Inverse Parameter Identification of Inhomogeneous SMC Composites, in: *Advances in Mechanics of Materials and Structural Analysis. Advanced Structured Materials*, volume 80, 2018, pp. 329–342. doi:10.1007/978-3-319-70563-7_{_}15.